Journal of Materials Chemistry A

High-performance Ruddlesden-Popper perovskite oxide with in-situ exsolved nanoparticles for direct CO2 electrolysis

Journal:	*Journal of Materials Chemistry A*
Manuscript ID	TA-ART-07-2023-004122.R1
Article Type:	Paper
Date Submitted by the Author:	17-Aug-2023
Complete List of Authors:	Park, Ka-Young; University of South Carolina, Mechanical Engineering Lee, Taehee; University of South Carolina, Mechanical Engineering Wang, Wanhua; University of South Carolina, Mechanical Engineering Li, Haixia; University of South Carolina, Mechanical Engineering Chen, Fanglin; University of South Carolina, Mechanical Engineering

ARTICLE

High-performance Ruddlesden-Popper perovskite oxide with in-situ exsolved nanoparticles for direct CO_2 electrolysis

Received 00th January 20xx,
Accepted 00th January 20xx

DOI: 10.1039/x0xx00000x

Ka-Young Park [a], Taehee Lee [a], Wanhua Wang [a], Haixia Li [a], and Fanglin Chen [a]

Carbon dioxide (CO_2) is one of the principal greenhouse gases accountable for global warming and extreme climate changes. Electrochemically converting CO_2 into carbon monoxide (CO) is a promising approach for CO_2 utilization in achieving industrial decarbonization. High-temperature CO_2 electrolysis via solid oxide electrolysis cells (SOECs) has great potentials, including high-energy efficiency, fast electrode kinetics, and competitive cost, however, this technology still has challenges associated with developing highly active, robust CO_2 electrode for SOECs. We report a novel Ruddlesden-Popper structured $Pr_{1.2}Sr_{0.8}Mn_{0.4}Fe_{0.6}O_{4-\delta}$ (RP-PSMF) with in-situ exsolved Fe nanoparticles as CO_2 electrode in SOECs for direct CO_2 conversion to CO. The mechanism of CO_2 electrolysis is studied by using the distribution of relaxation times method from the electrochemical impedance spectroscopy. $La_{0.8}Sr_{0.2}Ga_{0.8}Mg_{0.2}O_{3-\delta}$ (LSGM)-electrolyte supported SOECs with RP-PSMF cathode have achieved exceptionally high current densities of 2.90, 1.61, 0.91, and 0.48 $A{\cdot}cm^{-2}$ under an applied voltage of 1.5 V at 800, 750, 700, and 650°C, respectively. Moreover, SOECs with RP-PSMF cathode have exhibited a stable electrolysis performance for 100 h under a current cycling operation. These results suggest that RP-PSMF with exsolved Fe nanoparticles is a highly promising cathode for high-temperature direct CO_2 electrolysis cells.

Introduction

Controlling carbon dioxide (CO_2) emissions has become an inevitable grand challenge in order to mitigate the unpredictable and threatening climate changes resulting from global warming. The global lockdown associated with the coronavirus disease (COVID-19) pandemic has reduced CO_2 emissions considerably since human-made greenhouse gas activities have been temporarily halted or slowed down, which gives an opportunity to investigate the impact of CO_2 emission reduction on human beings and the environment.[1–3] Consequently, the strategies of CO_2 capture, utilization, and storage become further considered as approaches in order to actualize net-zero carbon emissions.[4,5]

The electrochemical method has gained intensive attention as a promising approach for reducing CO_2 emissions. For example, CO_2 can be directly converted into carbon monoxide (CO), an important industrial gas that has many applications in bulk chemical production.[4,6,7] Furthermore, the electrochemical CO_2 conversion can be an energy storage method for the excess electrical energy produced from intermittent renewable energy sources, such as solar, wind, and tide.[8–11] Thus, the capability of utilizing CO_2 can play a significant role enabling us toward a more sustainable economy in the post-COVID-19 era.

For CO_2 to CO conversion via the electrochemical process, solid oxide electrolysis cells (SOECs) have great potentials owing to several advantages including environmental-friendliness, high-energy conversion efficiency, fast electrode kinetics, competitive cost, *etc*.[4,7] In principle, anode catalysts used for solid oxide fuel cells (SOFCs) can be potential candidates as cathode catalysts in SOECs. SOFCs have significantly developed materially and technologically during the last several decades and the most common anode for SOFCs, nickel metal (Ni)-based cermet (e.g., Ni-yttria stabilized zirconia (YSZ)) has conventionally been used as a cathode catalyst of SOECs due to the excellent catalytic properties toward water (H_2O) splitting reaction, however, the Ni-based cermet is quickly degraded by re-oxidation of Ni metal grains in oxidizing conditions such as pure CO_2 and/or carbon deposition when exposed to carbon containing atmosphere,[12–16] thereby requiring protective gases such as CO and hydrogen (H_2) for CO_2 electrolysis operation with the Ni-based cermet. However, using protective gases will incur additional operational cost, add complexity to the high-temperature direct CO_2 electrolysis cell (CO_2 SOEC) system design, and reduce reliability of the overall CO_2 electrolysis system.

Recently, extensive efforts have been devoted to exploring alternative cathode catalysts with high catalytic activity for CO_2 SOECs to replace the Ni-based cermet. Perovskite-based oxides are attractive candidates for the cathode catalyst of CO_2 SOECs due to their acceptable electrical conductivity, redox stability, and coking resistance.[12,17,18] Particularly, ferrite-containing perovskites, such as $(La,Sr)(Cr,Fe)O_3$, $(La,Sr)(Fe,Mn)O_3$, and $Sr(Fe,Mo)O_3$, present high electrochemical performance as both anode and cathode materials.[19–21] For example, $LaTiO_{3-\delta}$-based perovskites have demonstrated good electrocatalytic activity via surface modification with exsolved iron (Fe) nanoparticles.[22] Although these developed perovskites show promising potentials, they still have limitations compared to the conventional Ni-YSZ cermet in terms of electrical conductivity and/or catalytic activity.[23,24] Moreover, some perovskites completely decompose into several secondary phases in low

[a] Department of Mechanical Engineering, University of South Carolina, Columbia, SC 29208

† Footnotes relating to the title and/or authors should appear here.
Electronic Supplementary Information (ESI) available: [details of any supplementary information available should be included here]. See DOI: 10.1039/x0xx00000x

oxygen partial pressure (P_{O_2})[25] such as CO gas (the product from direct CO_2 electrolysis cell), thereby raising concerns about the long-term stability of the perovskite-type cathodic catalysts for direct CO_2 electrolysis.

The Ruddlesden-Popper (RP) structure, also known as K_2NiF_4 structure, has been widely investigated as cathode materials in SOFCs because RP-structured oxides possess a high oxygen ion exchange rate and much higher phase stability than ferrite-containing perovskites.[26–29] Nevertheless, there have been very limited studies on application of RP-structured oxides as anode materials for SOFCs, while for CO_2 electrolysis RP-structured oxides are rarely reported as a cathodic catalyst,[30] which might be due to poor catalytic activity in reducing atmosphere as in SOFCs, or low catalytic activity in the oxidizing atmosphere as in direct CO_2 electrolysis. For example, $La_{0.6}Sr_{1.4}MnO_{4-\delta}$ has been reported to possess high chemical stability, but shows poor electrochemical activity in reducing atmosphere.[29] Therefore, for direct CO_2 electrolysis, it is of great importance to develop RP structured catalysts which possess good catalytic activity and long-term chemical stability at the same time.

Surface modification of RP-structured oxides may provide a viable approach to obtain both catalytic activity and chemical stability for SOEC applications. Impregnation is a conventional method to create active metal nanoparticles on the surface of matrix oxide, which contributes to enhancement of the catalytic performance of ceramic-based catalysts.[31-33] A number of reports have demonstrated that CO_2 electrolysis performance can be significantly enhanced when introducing transition metal particles including Ni, copper (Cu), and iron (Fe) on the perovskite catalysts.[34-36] However, due to the agglomeration of impregnated particles, severe performance degradation of the impregnated electrodes has been a major issue to be resolved.

Another approach for surface modification is an *in-situ* exsolution method. During the *in-situ* exsolution process, dopant cations diffuse to the surface to form metallic nanoparticles anchored on the surface of matrix oxide, resulting in uniformly dispersed metallic nanoparticles well-bonded to the matrix with a strong interaction between nanoparticles and oxides, potentially mitigating the agglomeration phenomena.[31, 37-39] The *in-situ* exsolution process has been shown great effectiveness to improve electrochemical properties as the anode material for SOFC and high catalytic activity with good stability as the cathode material for CO_2 SOECs.[7,40-43]

In this study, we have developed a novel RP-structured catalyst as the CO_2 SOEC cathode via the *in-situ* exsolution process. By heat-treating at 800°C in a reducing atmosphere, perovskite $Pr_{0.6}Sr_{0.4}Mn_{0.2}Fe_{0.8}O_{3-\delta}$ (PSMF) is transformed into the RP-structured $Pr_{1.2}Sr_{0.8}Mn_{0.4}Fe_{0.6}O_{4-\delta}$ (RP-PSMF) with *in-situ* exsolved metallic nanoparticles. The phase transformation phenomenon is examined by analyzing crystal structure, microstructure, oxidation states, and thermal behavior of the perovskite PSMF and the RP-structured PSMF. Electrochemical catalytic activity of RP-PSMF is evaluated by measuring direct CO_2 electrolysis performance and the reaction mechanisms are investigated by using distribution of relaxation times (DRT) method. Moreover, the long-term stability test for direct CO_2 electrolysis is performed by using electrolyte-supported solid oxide cells with the RP-PSMF cathode catalyst.

Experimental

Material synthesis

PSMF powder was synthesized via the sol-gel process. $Pr(NO_3)_3{\cdot}9H_2O$ (Sigma-Aldrich), $Sr(NO_3)_2$ (Sigma-Aldrich), $Mn(NO_3)_2{\cdot}4H_2O$ (Sigma-Aldrich) and $Fe(NO_3)_3$ $9H_2O$ (Sigma-Aldrich) were used as the precursor chemicals. The metal nitrates were dissolved in deionized (DI) water with stirring. The nitrate solution, citric acid (Sigma-Aldrich) and ethylenediaminetetraacetic acid (EDTA, Sigma-Aldrich) were mixed with a molar ratio of 1.0: 1.5: 1.0. The mixture solution was heated at 80°C on a hotplate under constant stirring until the solution changed to a gel, and the gel was subsequently heated at 400°C until self-ignition. The combusted powder was collected, pulverized, and then calcined at 1100°C for 5 h in air. The as-synthesized PSMF powder was heat-treated in H_2 at 800°C for 2 h to obtain RP-PSMF powder for the XRD analysis.

Cell fabrication

$La_{0.8}Sr_{0.2}Ga_{0.8}Mg_{0.2}O_{3-\delta}$ (LSGM), $La_{0.6}Sr_{0.4}Co_{0.2}Fe_{0.8}O_{3-\delta}$ (LSCF) and $Gd_{0.2}Ce_{0.8}O_{2-\delta}$ (GDC) powders were obtained from Fuelcellmaterials (OH, USA). For the CO_2 SOECs, the LSGM electrolyte substrates were fabricated by using a tape-casting method. The LSGM slurry was prepared by a ball-milling machine. LSGM powder was added into toluene (Aldrich) and ethanol (Aldrich) mixture solution with fish oil as a dispersant and mixed for 24 h. Polyvinyl butyral (PVB, Sigma-Aldrich), polyethylene glycol (PEG10000, Sigma-Aldrich), and benzyl butyl phthalate (BBP, Alfa Aesar) were added to the LSGM suspension as binders and plasticizers, and mixed for another 24 h. After degassing for 5 min in vacuum with stirring, the LSGM slurry was cast onto the polyester mylar film by using a doctor blade on a bench-top tape caster (Richard E. Mistler, Inc., USA) and dried in air at room temperature for 12 h. The LSGM green tape was punched into 15 mm circular disks and then sintered at 1450°C for 6 h. The composite PSMF-GDC cathode and LSCF-GDC anode (60:40 wt.% ratio) inks were prepared with a terpinol-based binder by using an agate mortar and pestle. The electrode inks were screen-printed onto each surface of the LSGM electrolyte substrate, the single cells were gently dried by an infrared heat lamp (250W, Philips), and then the cells were sintered at 1000°C for 2 h. Silver (Ag) wires were attached as current lead wires to both the anode and cathode sides of the prepared cells using platinum (Pt) paste and then fired at 900°C for 2 h. Single cells were mounted in a home-made alumina cell tester using a high-temperature ceramic adhesive (Ceramabond 552, Aremco) as sealant.

To evaluate the overpotentials contributed from different cathode materials, PSMF and RP-PSMF, a three-electrode method was employed by using a symmetrical cell configuration. For the symmetrical cells, the LSGM electrolyte supports were prepared by using an uniaxial die pressing method and sintered at 1450°C for 6 h. Then, the composite

PSMF-GDC) electrodes were deposited via the screen-printing method onto both sides of the LSGM electrolyte, and fired at 1000°C for 2 h. Assemblies of Pt wire and mesh were prepared as a current collector by using a spot-welder (SUNKKO 709A) and attached using a gold (Au) paste for working and counter electrodes. The reference electrode is a Pt wire attached using the Au paste to the circumference of the LSGM electrolyte support. Then, the composite RP-PSMF-GDC electrodes were obtained via the *in-situ* exsolution process. The symmetrical cells were exposed to H_2 atmosphere at 800°C for 1 h and the overpotential measurement was performed with feeding pure CO_2 atmosphere.

Characterizations

The crystal structures of the synthesized PSMF and RP-PSMF powders were investigated by powder X-ray diffraction (XRD, MiniFlex II, Rigaku) using Cu Kα radiation in the 2θ range of 20° to 80°. Rietveld refinement of the obtained XRD results was performed to analyze the crystal structure of the materials in detail by using GSAS-II software.[44] The oxidation states of transition elements were analyzed by X-ray photoelectron spectroscopy (XPS, VersaProbe III spectrometer, PHI). The microstructures of the synthesized powders and single cells were analyzed using field emission-scanning electron microscopy (FE-SEM, Gemini500, Zeiss).

Thermal gravimetric analysis (TGA, STA 449 F3 Jupiter®, NETZSCH) was performed on PSMF powder from 25 to 900°C under H_2 with a flow rate of 40 mL min^{-1} and a ramping rate of 5°C/min. The conversion ratio of CO_2/CO outlet gas from the cathode side was analyzed by using a gas chromatograph (GC; 7890A, Agilent).

Electrochemical performance of the single cells was measured by using Versa STAT 3-400 electrochemical workstation. Current– voltage (I-V) polarization curves were obtained with linear scan voltammetry mode. Electrochemical impedance spectra (EIS) were measured at open circuit voltage (OCV) on single cells with a frequency range of 10^6 to 0.01 Hz and an AC amplitude of 10 mV.

The overpotentials of the cathode materials were obtained from EIS results. The EIS measurement related to CO_2 reduction reaction was performed in pure CO_2 atmosphere while applying the DC current in the temperature range from 650°C to 800°C in a 50°C interval. The obtained polarization resistance is integrated over current density (J) to obtain overpotential (η). The details on this method can be found in the Ref. 45.

Results and discussion

Crystal structure, oxidation state, and microstructure analysis for the *in-situ* exsolution process

In-situ exsolution is a promising method to enhance the catalytic activity of oxide-based electrodes. The crystal structure and exsolution behavior were analyzed by using XRD profiles of the as-calcined PSMF in air at 1100°C and as-reduced RP-PSMF in H_2 at 800°C as shown in Figure 1a. The observed

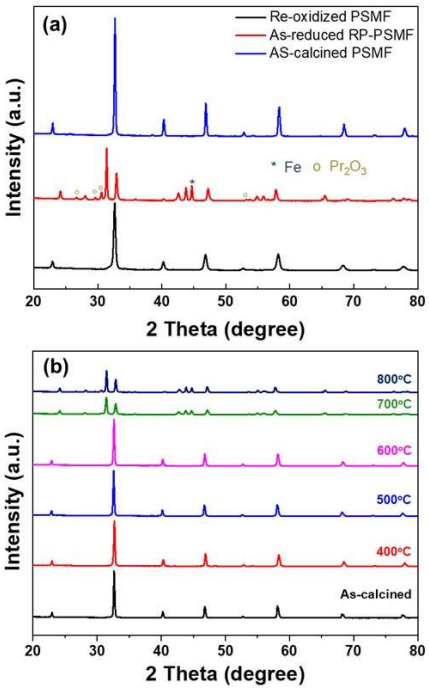

Figure 1. XRD characterization for the crystalline structure of the synthesized powders and the critical temperature relevant to the *in-situ* exsolution process. XRD patterns of as-calcined PSMF in air, as-reduced RP-PSMF in H_2, and re-oxidized PSMF in CO_2 (a), and PSMF heat-treated at different temperatures in H_2 (b).

phase transformation was reversible. Upon annealing the as-reduced RP-PSMF in an oxidizing atmosphere (pure CO_2), the RP-PSMF transformed back into the simple perovskite PSMF (re-oxidized PSMF) phase; the XRD spectra of both PSMF and RP-PSMF were further analyzed to index the crystal structures via Rietveld refinement, as shown in Figure S1. The XRD peaks of as-calcined PSMF can be indexed to the perovskite phase as the $Pnma$ space group in the orthorhombic crystal system. When exposed to low P_{O_2} atmosphere, the PSMF was transformed to the RP-phase (RP-PSMF), indexed as $I4/mmm$ space group in the tetragonal system, with additional diffraction peaks corresponding to metallic iron (Fe) and praseodymium oxide (Pr_2O_3) phases. The weighted profile R-factors (R_{wp}) were 3.82% and 5.93% for PSMF and RP-PSMF, respectively, indicating that the results from the Rietveld refinement are statistically reliable. The lattice parameters were summarized in Table 1.

The phase transformation reaction from PSMF to RP-PSMF with the exsolved phases can be represented by the following equation:

$$Pr_{0.6}Sr_{0.4}Mn_{0.2}Fe_{0.8}O_{3-\alpha} + \left(1+\frac{\gamma}{2}+\frac{3\beta}{4}-\alpha\right)H_2 \rightarrow \frac{1}{2}Pr_{1.2-\beta}Sr_{0.8}Mn_{0.4}Fe_{0.6}O_{4-\gamma} + \frac{1}{2}Fe + \frac{\beta}{4}Pr_2O_3 + (1+\frac{\gamma}{2}+\frac{3\beta}{4}-\alpha)H_2O \quad (1)$$

These exsolved metallic Fe and Pr_2O_3 have the potential to enhance the electrochemical reactions at the CO_2 electrode. It is well-known that metallic nanoparticles serve as active sites for electrochemical reactions,[6,7,40,46] effectively decomposing the adsorbed CO_2 (or carbonate species) into CO and oxygen

Table 1. Lattice parameters of the perovskite PSMF and RP-PSMF via in-situ exsolution in H_2 at 800°C.

Materials	Lattice system	Space group	a (Å)	b (Å)	c (Å)	Volume (Å^3)	R_{wp}(%)
PSMF	orthorhombic	$Pnma$	5.47514	5.49635	7.74400	233.042	3.82
RP-PSMF	Tetragonal	$I4/mmm$	3.84668	3.84668	12.72874	188.346	5.93

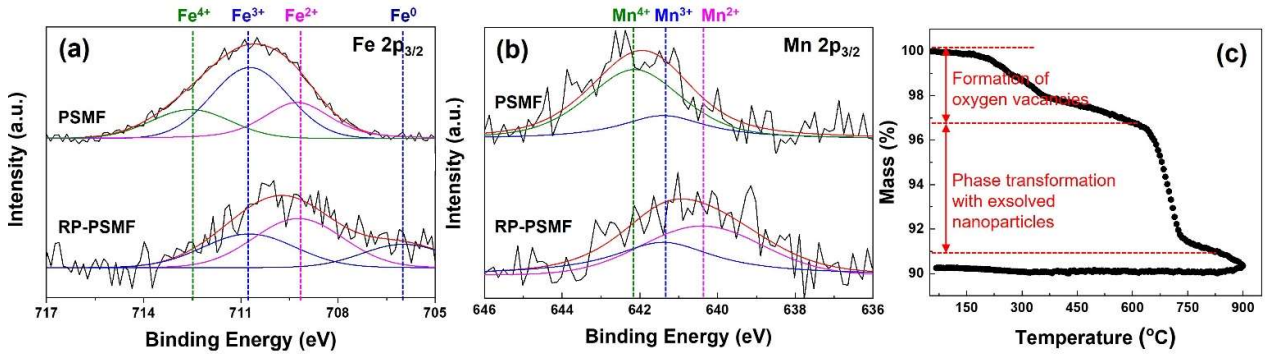

Figure 2. Oxidation state changes of Fe, Mn, and O elements during the *in-situ* exsolution process. XPS spectra of Fe $2p_{3/2}$ (a) and Mn $2p_{3/2}$ (b) corresponding to PSMF and RP-PSMF. Temperature-dependent phase transformation has been analyzed using TGA (c).

ions.[50,61,63] It has also been reported that Pr_2O_3 promotes the charge transfer process and can reduce the interfacial resistance of the fuel electrode.[47–49] Moreover, RP structured oxides facilitate oxygen ion migration due to the interstitial oxygen species in the lattice.[29] This phase transformation was clearly dependent on the temperature (Figure 1b). To evaluate the critical temperature for *in-situ* exsolution, as-calcined PSMF was heat-treated for 2 h at 400, 500, 600, 700, and 800°C in H_2 atmosphere, respectively. When exposed to H_2 at different-temperatures, it was clearly demonstrated that the perovskite PSMF was transformed to RP-PSMF in the temperature range between 600 and 700°C. The electrochemical properties including the catalytic activity of the perovskite structure tend to be determined by the oxidation state of the B-site element in the perovskites.[42,50]

XPS spectra show changes in the oxidation states of two B-site elements (Fe and Mn) in the PSMF and RP-PSMF (Figure 2a). The baseline has been subtracted from each original spectra for peak deconvolution. The binding energy (E_B) of the Fe $2P_{3/2}$ spectrum composes of Fe^0, Fe^{2+}, Fe^{3+}, and Fe^{4+} spectra. E_B values of three subpeaks are theoretically 706.9, 709.4, 710.7, and 712.4 eV, respectively.[40,51,52] The center of measured E_B was 710.7 eV for PSMF and 709.2 eV for RP-PSMF, respectively. XPS spectra indicate that PSMF has three oxidation states of $Fe^{2+/3+/4+}$ and Fe^{3+} is a dominant state (46%), while RP-PSMF has Fe^0 subpeak related to Fe nanoparticles and Fe^{2+} is a dominant state (47%) among three oxidation states.

Mn $2P_{3/2}$ spectra showed a similar change in the oxidation states (Figure 2b). Theoretical E_B values of Mn $2P_{3/2}$ spectra are 640.4, 641.4, and 642.1 eV for Mn^{2+}, Mn^{3+}, and Mn^{4+} subpeaks, respectively.[40,52] The center of the measured E_B for PSMF was 641.9 eV and decreased to 640.9 eV (E_B for RP-PSMF) when exposed to the low P_{O_2} atmosphere. Mn^{4+} was a dominant state (72%) between $Mn^{3+/4+}$ states in the PSMF, however, Mn^{2+} became a dominant state (54%) in the RP-PSMF after the reduction in 5% H_2. Considering both XRD and XPS data, it can be seen that Fe nanoparticles were exsolved when PSMF was transformed to RP-PSMF in the reducing atmosphere, while Fe and Mn ions that remained in the lattice were further reduced during the *in-situ* exsolution process.

Based on the XPS results, it indicated that the reduced oxidation states of Fe ($Fe_{Fe}^{3+} \rightarrow Fe_{Fe}^{2+}$) and Mn ($Mn_{Mn}^{4+} \rightarrow Mn_{Mn}^{3+}$) can promote formation of oxygen vacancies during the *in-situ* exsolution processes by using the following equations:

$$2Fe_{Fe}^{3+} + O_O^{\times} + H_2 \rightarrow 2Fe_{Fe}^{2+} + H_2O + V_O^{\cdot\cdot} \quad (2)$$

$$2Mn_{Mn}^{4+} + O_O^{\times} + H_2 \rightarrow 2Mn_{Mn}^{3+} + H_2O + V_O^{\cdot\cdot} \quad (3)$$

The mass change of the PSMF in low P_{O_2} atmosphere with increasing temperature has also demonstrated that oxygen defect formation and phase transformation are temperature-dependent processes. To measure the mass change of the PSMF in the reducing atmosphere, TGA was performed over the temperature range from 25 to 900°C (Figure 2d). The mass of PSMF decreased gradually from 200 to 450°C, indicating that oxygen defect formation associated with equations (2) and (3) is the dominant process during the initial stage of mass loss because the perovskite structure has been maintained in this low-temperature range (Figure 1b). Significant mass loss occurred in the temperature range from 650 to 750°C, and it could be closely attributed to the phase transformation from perovskite to RP structure with exsolved nanoparticles related to equation (1). These results indicated that the *in-situ* exsolution process could induce not only the exsolution of nanoparticles but also the promotion of oxygen vacancy formation, both of which are instrumental in enhancing direct CO_2 electrolysis performance.

The nanoparticles on the surface of RP-PSMF were clearly demonstrated via the SEM-EDX analysis. EDX spectra with line

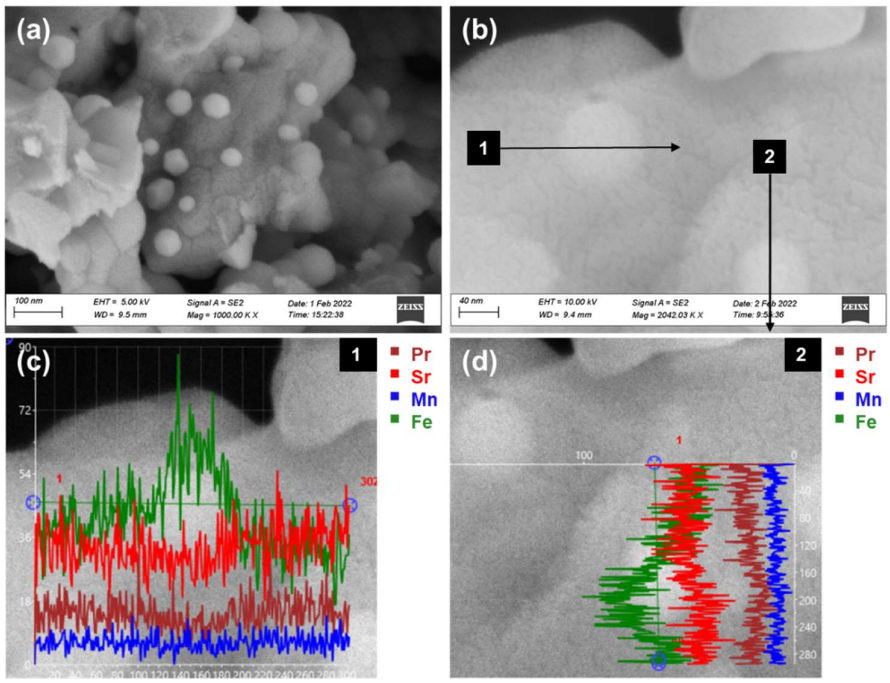

Figure 3. *In-situ* exsolved nanoparticles on the RP-PSMF observed through SEM (a-b) and the elements of the nanoparticles analyzed by using EDX line scanning mode (c-d).

scanning mode presents that the *in-situ* exsolution process creates Fe nanoparticles. Figure 3a shows the microstructure of the CO_2 electrode in the LSGM-supported cell (Configuration: RP-PSMF-GDC|LSGM|LSCF-GDC) after direct CO_2 electrolysis operation. In the SEM image, the isolated nanoparticles were brighter than their matrix of RP-PSMF, whose average particle size with standard deviation was 45.89 ± 11.32 nm in diameter. EDX analyses with line scanning mode were performed twice (Figure 3b-d). The green signals of the Fe element were intensified when EDX scanning lines 1 and 2 passed through the isolated particles, whereas the other signals of the Pr (brown), Sr (red), and Mn (blue) elements were not changed evidently during the EDX scanning. This result indicates that the nanoparticles are Fe-rich compounds, and by combining XRD and XPS data, it is solidified that Fe nanoparticles are successfully formed over the RP-PSMF matrix particles via the *in-situ* exsolution process.

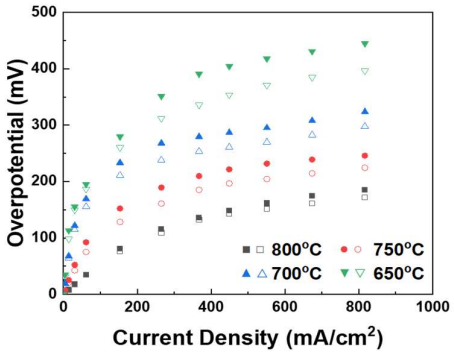

Figure 4. The plot of overpotential vs. current density of the symmetrical cells with different electrodes: PSMF-GDC (Solid) and RP-PSMF-GDC (Open) electrodes.

CO_2 electrolysis performance of the RP-PSMF catalyst

Figure 4 shows the typical plot of the overpotential (η) vs. the current density (J) of the symmetrical cells with PSMF-GDC and RP-PSMF-GDC electrodes. The overpotential of the RP-PSMF-GDC electrode is lower than that of the PSMF-GDC electrode in the measured range of current density. However, the difference in overpotential becomes more pronounced as the temperature decreases, suggesting that RP-PSMF exhibits greater catalytic activity for the CO_2 reduction reaction compared to PSMF, particularly at lower operating temperatures. To further characterize the electrochemical catalytic activity of RP-PSMF for direct CO_2 electrolysis, the current-voltage (*I-V*) polarization curves were obtained by using the LSGM-supported cell (Cell configuration: PSMF-GDC | LSGM| LSCF-GDC as shown in Figure S2). For *in-situ* exsolution process, the PSMF-GDC in the fuel electrode was transformed into RP-PSMF-GDC by feeding H_2 for 1 h at 800°C prior to the *I-V* polarization measurement. The OCV of the cell in the fuel cell mode (hydrogen-air system) was 1.07 V as shown in Figure S3 and very close to the theoretical OCV value (1.10 V) at 800°C,[54] indicating that the cell was properly sealed. After the reduction process, pure CO_2 was fed into the fuel electrode to evaluate the electrochemical performance for direct CO_2 electrolysis. I-V polarization curves at different temperature show two slopes of profiles. In the initial stage (low current density range), the cell voltage increased rapidly in response to changes in current density. This might be due to the activation losses related to CO_2 reduction reaction ($2CO_2 \rightarrow 2CO + O_2$). After the initial stage, the I-V curves were changed to lower slope, indicating that this region may be primarily associated with ohmic losses. Furthermore, the reaction rate or current density of CO_2

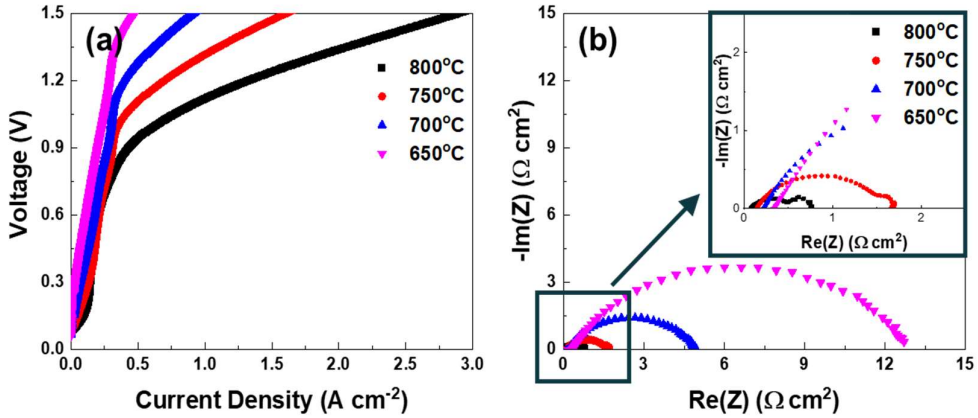

Figure 5. Characterization of pure CO_2 electrolysis performance at various operating temperatures: (a) I-V polarization curves, and (b) EIS profiles at the OCV conditions.

electrolysis was accelerated at elevated temperatures due to the higher conductivity of electrolyte and better catalytic activity of electrodes. When the applied potential was at 1.5 V, the current densities of the single cell were 2.90, 1.61, 0.91, and 0.48 A·cm^{-2} at the operating temperatures of 800, 750, 700, and 650°C, respectively (Figure 5a). To the best of our knowledge, a current density of 2.90 A·cm^{-2} is the highest value compared to the previous reports for pure CO_2 electrolysis at 800°C under similar testing conditions (Table 2).

EIS measurements were performed at V_{oc} when feeding pure CO_2 to the fuel electrode (Figure 5b). The ohmic resistance (R_{ohm}) is the first x-intercept of the semi-circle spectra in the high-frequency region, which typically accounts for ionic conduction passing through the electrolyte, electronic conduction within the cell component, and contact resistance,[63,64] while the total polarization resistance (R_p) is calculated by subtracting the R_{ohm} from the total resistance estimated by the second x-intercept of the spectra in the low-frequency region, which is attributed to the charge transfer reaction and mass transfer steps at interfaces between electrode and electrolyte.[65] The current densities at 1.5 V, R_{ohm}, and R_p at 800, 750, 700, and 650°C are summarized in Table 3. The R_p values of the cell decreased obviously with the elevated temperature (Figure 5b), indicating that higher catalytic activity of electrodes at higher temperatures. As the R_p of the EIS profile is roughly composed of high-frequency resistance corresponding to the charge transfer reaction and low-frequency resistance related to the diffusion steps in the electrode region,[7] the DRT analysis was employed to correctly distinguish the electrode processes for CO_2 reduction.

Table 2. Current density at 1.5 V and total polarization resistance (R_p) at OCV for direct CO_2 electrolysis performance of various fuel electrodes at 800°C.

Fuel electrode	Electrolyte (thickness)	Oxygen electrode	Atmosphere	R_p (Ω·cm^2)	Current density at 1.5V (A·cm^{-2})	refs
Ag-GDC	YSZ (130 μm)	LSM	CO_2	~1.25	~ 0.675	[55]
SFMgM	LSGM/LDC (200 μm / 5 μm)	LSCF-SDC	CO_2	1.25	1.4	[56]
LSFT	LSGM	LSCF-GDC	CO_2	-	1.11	[57]
SFRuM-GDC	LSGM/LDC (260 μm)	BSCF-GDC	CO_2	-	~1.87	[58]
SFMM-SDC	LSGM (400 μm)	SFMM-SDC	CO_2	0.58	1.35	[59]
LSFN	GDC/YSZ/GDC (400 μm)	LSFN	CO_2	0.91	~0.65	[60]
SMFN-SDC	LSGM/SDC (180 μm)	LSM-YSZ	CO_2	-	2.16	[61]
LCFN-GDC	GDC/YSZ/GDC (300μm)	LSCF-GDC	CO_2	0.7	~0.8	[62]
RP-PSMF-GDC	LSGM (190 μm)	LSCF-GDC	CO_2	0.679	2.90	This work

LSM: $La_{0.7}Sr_{0.3}MnO_{3-\delta}$; SDC: $Sm_{0.2}Ce_{0.8}O_{2-\delta}$; BSCF: $Ba_{0.5}Sr_{0.5}Co_{0.8}Fe_{0.2}O_{3-\delta}$; SFMgM: $Sr_2FeMo_{2/3}Mg_{1/3}O_{6-\delta}$; LSFT: $La_{0.3}Sr_{0.7}Fe_{0.9}Ti_{0.1}O_{3-\delta}$; SFRuM: $Sr_2Fe_{1.4}Ru_{0.1}Mo_{0.5}O_{6-\delta}$; SFMM: $Sr_2Fe_{1.4}Mn_{0.1}Mo_{0.5}O_{6-\delta}$; LSFN: $La_{0.6}Sr_{0.4}Fe_{0.8}Ni_{0.2}O_{3-\delta}$; SFMN: $Sr_{1.9}Fe_{1.5}Mo_{0.4}Ni_{0.1}O_{6-\delta}$; LCFN: $La_{0.6}Ca_{0.4}Fe_{0.8}Ni_{0.2}O_{3-\delta}$

Table 3. Current densities, ohmic and total polarization resistances at OCV at different temperatures of 800, 750, 700, and 650°C.

Temp. (°C)	Current density at 1.5 V (A·cm^{-2})	R_{ohm} (Ω·cm^2)	R_p (Ω·cm^2)
800	2.90	0.083	0.679
750	1.61	0.144	1.518
700	0.91	0.214	4.627
650	0.48	0.342	12.365

DRT analysis for the mechanisms of CO_2 reduction reaction

To investigate CO_2 reduction process under the operating conditions, EIS measurements were also conducted while applying various potentials from 0.4 to 1.4 V and the EIS results were deconvoluted by using the DRT analysis as shown in Figure 6. In the DRT plots, four peaks denoted by P1, P2, P3, and P4 from high-frequency to low-frequency correspond to the electrocatalytic CO_2 reduction reaction, involving four elementary electrode processes:[4,66]

- P1 (frequency = 1-10 kHz): oxygen ion (O^{2-}) transfer through the LSGM electrolyte
- P2 (frequency = 10-1000 Hz): oxygen evolution reaction ($O^{2-} \rightarrow O_2$) in the air electrode
- P3 (frequency = 1-10 Hz): CO_2/CO conversion at the fuel electrode
- P4 (frequency < 1 Hz): CO_2 diffusion and/or adsorption/desorption at the fuel electrode

P3 corresponding to CO_2/CO conversion was rarely initiated with low potentials because this process theoretically requires 0.98 V of thermodynamic equilibrium potential at 800°C to promote CO_2 reduction reaction ($2CO_2 \leftrightarrow 2CO + O_2$), while CO_2 diffusion and/or adsorption/desorption processes act as a rate-determining step and the peak area of P4 is significantly decreased with increasing applied potentials, indicating that this process became facilitated as shown in Figure 6a.

Thus, in the low potential regions (0.4 to 0.8 V), CO_2 molecules are diffused and adsorbed onto the lattice oxygen ($O^x_{O,s}(V^{\cdot\cdot}_{O,s})$) adjacent to the surface oxygen vacancies ($V^{\cdot\cdot}_{O,s}$) as a form of carbonate intermediate ($(CO_3)^-_{s,ad}$) as following equation (4);

$$CO_2 + e^- + O^x_{O,s}(V^{\cdot\cdot}_{O,s}) \leftrightarrow (CO_3)^-_{s,ad} \quad (4)$$

Subsequently, the carbonate intermediate has to consume another electron and be incorporated into the surface oxygen vacancies for dissociation of oxygen ion and formation of lattice oxygen ($O^x_{O,s}$) in order to CO production (P3 process) as following equation (5);

$$(CO_3)^-_{s,ad} + e^- + V^{\cdot\cdot}_{O,s} \leftrightarrow CO + 2O^x_{O,s} \quad (5)$$

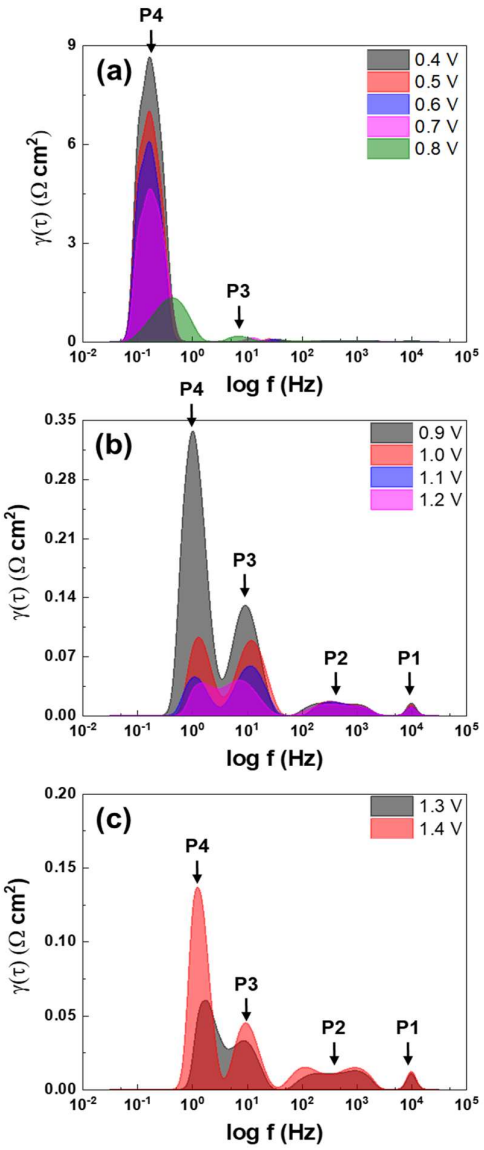

Figure 6. DRT analysis of the LSGM electrolyte-supported cell (Configuration: RP-PSMF-GDC|LSGM|LSCF-GDC) at 800°C while feeding 100% CO_2 to the cathode and exposing the anode to ambient air. EIS dataset has been obtained under different applied potentials: (a) 0.4 - 0.8 V, (b) 0.9 – 1.2 V, and (c) 1.3 and 1.4 V.

However, CO production in the low potential regions is rarely occurred due to insufficient applied potential to overcome the activation barrier for the CO_2 reduction reaction. When applying intermediate potentials (0.9 to 1.2 V), the overall CO_2 reduction reactions were significantly accelerated due to reduced resistances of the P3 and P4 processes (Figure 6b). On the other hand, P1 and P2 processes were relatively insensitive reactions to changes in the applied potentials because oxygen ion conduction and oxygen exchange kinetics are materials properties strongly depending on temperature and oxygen partial pressure. At higher potentials (1.3 and 1.4 V), P3 and P4 processes became increased again (Figure 6c),

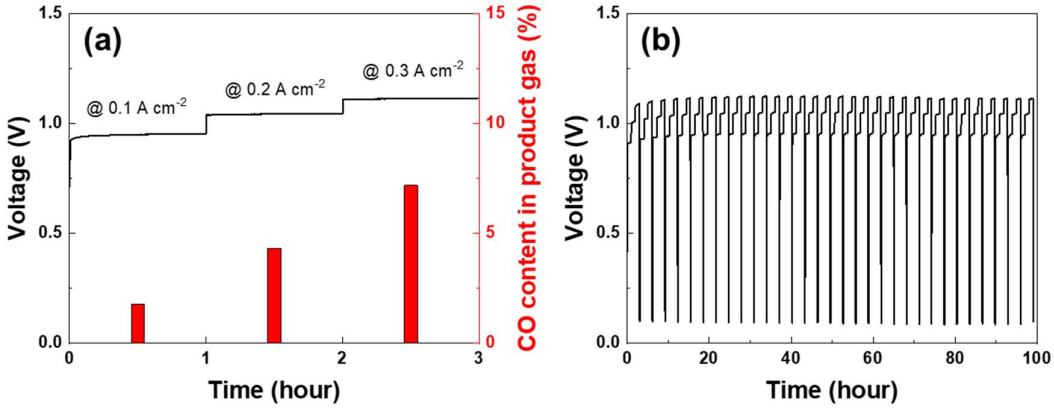

Figure 7. Voltage behavior and CO content in the product gas of the single cell at 800°C with applied current densities of 0.1, 0.2, and 0.3 A· cm^{-2} (a) and long-term stability test for 100 h under the current cycling operation from 0.1 to 0.3 A cm^{-2} (b).

indicating that the CO_2 reduction reaction begins to be affected by concentration polarization due to the lack of CO_2 molecules and/or active sites for CO_2 conversion at the triple phase boundary as a result of the high surface coverage of CO produced.

Long-term stability for direct CO_2 electrolysis cell

The cell with RP-PSMF cathode was stable over long-term operation at 800°C with cycling applied currents in pure CO_2 as shown in Figure 7. At 0.1, 0.2, and 0.3 A·cm^{-2} of applied current densities, CO contents in the product gas were 1.79, 4.32, and 7.19%, respectively, and the cell operation was stable without any voltage fluctuation (Figure 7a). When the applied current densities increased double or treble, the CO gas was produced more than the multiple of the current densities. It was because the faraday efficiency is enhanced with increasing current densities. At 0.1, 0.2, and 0.3 A·cm^{-2} of the current densities, the faraday efficiency was 70.5, 85.1, and 94.4 %, respectively. The faraday efficiency might be improved when the current density is increased. This is because CO_2 reduction reaction can be more facilitated due to the enhanced driving force resulting from higher current density, which is necessary to overcome high activation barrier of CO_2/CO conversion.

As shown in Figure 7b, the long-term stability test was conducted at 800°C in pure CO_2 with the current cycling operation; the applied current densities were increased step-by-step every hour from 0.1 to 0.3 A·cm^{-2} and corresponding voltages were around 0.9, 1.0, and 1.1 V, respectively, and then the applied current was removed immediately. This current cycling operation was repeated 32 times. During the electrolysis operation for ~100 h, the cell with RP-PSMF showed stable and periodical voltage profile even under the current cycling operation (Figure 7b).

The RP-PSMF with *in-situ* exsolved Fe nanoparticles showed great performance for electrochemical CO_2 reduction, which is remarkable compared to the previously reported values (Figure 6 and Table 2). Moreover, the developed RP-PSMF presented a stable voltage profile during the long-term operation even in a 100% CO_2 atmosphere (Figure 7), indicating that no protecting gas is required for CO_2 electrolysis even though some studies have still utilized CO gas to provide reducing atmosphere to stabilize CO_2 electrolysis operation.[4,7] Therefore, the developed RP-PSMF with nanoparticles can serve as a promising SOEC cathode material for direct CO_2 to CO conversion with great performance and stability.

Conclusions

RP-PSMF with Fe nanoparticles were synthesized via *in-situ* exsolution process by heat-treating PSMF in low P_{O_2} atmosphere and studied as cathode material for direct CO_2 electrolysis, resulting in great electrochemical activity and good stability. LSGM electrolyte-supported cell with RP-PSMF cathode achieved high electrolysis performance in pure CO_2 with a current density of 2.90 A·cm^{-2} at 800°C at 1.5V. Exposure to low P_{O_2} atmosphere at elevated temperature promotes phase transformation involving reduction of B-site elements (Fe^{2+} and Mn^{2+}) and oxygen vacancy formation, leading to enhanced catalytic activity for direct CO_2 electrolysis. In addition, RP-PSMF with *in-situ* exsolved Fe nanoparticles was a reliable and stable cathode material during the long-term stability test under the current cycling operation. These results demonstrate the *in-situ* exsolution process has a great potential to develop catalytic active materials with stability for direct CO_2 electrolysis reactions.

Conflicts of interest

There are no conflicts to declare.

Acknowledgements

Financial support from the U.S. Department of Energy (DE-EE0009427) and NASA EPSCoR (Grant # 80NSSC20M0233) is greatly appreciated.

Notes and references

1 C. Le Quéré, R. B. Jackson, M. W. Jones, A. J. P. Smith, S. Abernethy, R. M. Andrew, A. J. De-Gol, D. R. Willis, Y. Shan, J.

G. Canadell, P. Friedlingstein, F. Creutzig and G. P. Peters, Temporary reduction in daily global CO_2 emissions during the COVID-19 forced confinement, *Nat. Clim. Chang.*, 2020, **10**, 647–653.

2 Z. Liu, P. Ciais, Z. Deng, R. Lei, S. J. Davis, S. Feng, B. Zheng, D. Cui, X. Dou, B. Zhu, R. Guo, P. Ke, T. Sun, C. Lu, P. He, Y. Wang, X. Yue, Y. Wang, Y. Lei, H. Zhou, Z. Cai, Y. Wu, R. Guo, T. Han, J. Xue, O. Boucher, E. Boucher, F. Chevallier, K. Tanaka, Y. Wei, H. Zhong, C. Kang, N. Zhang, B. Chen, F. Xi, M. Liu, F. M. Bréon, Y. Lu, Q. Zhang, D. Guan, P. Gong, D. M. Kammen, K. He and H. J. Schellnhuber, Near-real-time monitoring of global CO_2 emissions reveals the effects of the COVID-19 pandemic, *Nat. Commun.*, 2020, **11**, 1–12.

3 J. C. Fyfe, V. V. Kharin, N. Swart, G. M. Flato, M. Sigmond and N. P. Gillett, Quantifying the influence of short-term emission reductions on climate, *Sci. Adv.*, 2021, **7**, 1–5.

4 S. Lee, M. Kim, K. T. Lee, J. T. S. Irvine and T. H. Shin, Enhancing Electrochemical CO_2 Reduction using $Ce(Mn,Fe)O_2$ with $La(Sr)Cr(Mn)O_3$ Cathode for High-Temperature Solid Oxide Electrolysis Cells, *Adv. Energy Mater.*, 2021, **11**, 2100339.

5 C. Sun, J. A. Alonso and J. Bian, Recent Advances in Perovskite-Type Oxides for Energy Conversion and Storage Applications, *Adv. Energy Mater.*, 2021, **11**, 2000459.

6 J. Zhu, W. Zhang, Y. Li, W. Yue, G. Geng and B. Yu, Enhancing CO_2 catalytic activation and direct electroreduction on in-situ exsolved Fe/MnOx nanoparticles from $(Pr,Ba)_2Mn_{2-y}Fe_yO_{5+\delta}$ layered perovskites for SOEC cathodes, *Appl. Catal. B Environ.*, 2020, **268**, 118389.

7 J. Choi, S. Park, H. Han, M. Kim, M. Park, J. Han and W. B. Kim, Highly efficient CO_2 electrolysis to CO on Ruddlesden-Popper perovskite oxide within situexsolved Fe nanoparticles, *J. Mater. Chem. A*, 2021, **9**, 8740–8748.

8 C. Zhu, S. Hou, X. Hu, J. Lu, F. Chen and K. Xie, Electrochemical conversion of methane to ethylene in a solid oxide electrolyzer, *Nat. Commun.*, 2019, **10**, 1–8.

9 X. Zhang, L. Ye, H. Li, F. Chen and K. Xie, Electrochemical Dehydrogenation of Ethane to Ethylene in a Solid Oxide Electrolyzer, *ACS Catal.*, 2020, **10**, 3505–3513.

10 V. Kyriakou, D. Neagu, G. Zafeiropoulos, R. K. Sharma, C. Tang, K. Kousi, I. S. Metcalfe, M. C. M. Van De Sanden and M. N. Tsampas, Symmetrical Exsolution of Rh Nanoparticles in Solid Oxide Cells for Efficient Syngas Production from Greenhouse Gases, *ACS Catal.*, 2020, **10**, 1278–1288.

11 L. Ye, X. Duan and K. Xie, Electrochemical Oxidative Dehydrogenation of Ethane to Ethylene in a Solid Oxide Electrolyzer, *Angew. Chemie*, 2021, **133**, 21914–21918.

12 X. Yue and J. T. S. Irvine, Alternative Cathode Material for CO_2 Reduction by High Temperature Solid Oxide Electrolysis Cells , *J. Electrochem. Soc.*, 2012, **159**, F442–F448.

13 A. Hauch, S. H. Jensen, S. Ramousse and M. Mogensen, Performance and Durability of Solid Oxide Electrolysis Cells, *J. Electrochem. Soc.*, 2006, **153**, A1741–A1747.

14 Y. Tao, D. Ebbesen and M. B. Mogensen, Carbon Deposition in Solid Oxide Cells during Co-Electrolysis of H_2O and CO_2, *J. Electrochem. Soc.*, 2014, **161**, F337–F343.

15 S. D. Ebbesen and M. Mogensen, Electrolysis of carbon dioxide in Solid Oxide Electrolysis Cells, *J. Power Sources*, 2009, **193**, 349–358.

16 Y. Shang, A. L. Smitshuysen, M. Yu, Y. Liu, X. Tong, P. S. Jørgensen, L. Rorato, J. Laurencin and M. Chen, 3D microstructural characterization of Ni/yttria-stabilized zirconia electrodes during long-term CO_2 electrolysis, *J. Mater. Chem. A*, 2015, **11**, 12245–12257.

17 D. Marrero-Loópez, J. Canales-Vázquez, J. C. Ruiz-Morales, A. Rodrígueza, J. T. S. Irvine and P. Núñez, Synthesis , sinterability and ionic conductivity of nanocrystalline La 2 Mo 2 O 9 powders, *Solid State Ionics*, 2005, **176**, 1807–1816.

18 V. Dusastre, S. TAO and J. T. S. IRVINE, A redox-stable efficient anode for solid-oxide fuel cells, *Mater. Sustain. Energy*, 2012, 259–262.

19 X. Kong, X. Zhou, Y. Tian, X. Wu, J. Zhang and W. Zuo, Niobium doped lanthanum calcium ferrite perovskite as a novel electrode material for symmetrical solid oxide fuel cells, *J. Power Sources*, 2016, **326**, 35–42.

20 T. H. Shin, S. Ida and T. Ishihara, Doped CeO_2-$LaFeO_3$ composite oxide as an active anode for direct hydrocarbon-type solid oxide fuel cells, *J. Am. Chem. Soc.*, 2011, **133**, 19399–19407.

21 T. Wei, X. Zhou, Q. Hu, Q. Gao, D. Han, X. Lv and S. Wang, A high power density solid oxide fuel cell based on nano-structured $La_{0.8}Sr_{0.2}Cr_{0.5}Fe_{0.5}O_{3-\delta}$ anode, *Electrochim. Acta*, 2014, **148**, 33–38.

22 S. Hu, L. Zhang, L. Cai, Z. Cao, Q. Jiang, W. Yu, Y. Wu, X. Zhu and W. Yang, Iron stabilized 1/3 A-site deficient La-Ti-O perovskite cathodes for efficient CO_2 electroreduction, *J. Mater. Chem. A*, 2020, **8**, 21053–21061.

23 S. P. Jiang, L. Liu, K. P. Ong, P. Wu, J. Li and J. Pu, Electrical conductivity and performance of doped $LaCrO_3$ perovskite oxides for solid oxide fuel cells, *J. Power Sources*, 2008, **176**, 82–89.

24 L. Lu, C. Ni, M. Cassidy and J. T. S. Irvine, Demonstration of high performance in a perovskite oxide supported solid oxide fuel cell based on La and Ca co-doped $SrTiO_3$, *J. Mater. Chem. A*, 2016, **4**, 11708–11718.

25 L. Zhu, B. Wei, Y. Zhang, Z. Lü, Z. Wang, X. Huang, Z. Cao, W. Jiang and Y. Li, Investigation on a novel composite solid oxide fuel cell anode with $La_{0.6}Sr_{0.4}Co_{0.2}Fe_{0.8}O_{3-\delta}$ derived phases, *Electrochim. Acta*, 2015, **160**, 89–93.

26 M. A. Laguna-Bercero, H. Monzón, A. Larrea and V. M. Orera, Improved stability of reversible solid oxide cells with a nickelate-based oxygen electrode, *J. Mater. Chem. A*, 2016, **4**, 1446–1453.

27 Y. Chen, B. Qian, G. Yang, D. Chen and Z. Shao, Insight into an unusual lanthanum effect on the oxygen reduction reaction activity of Ruddlesden-Popper-type cation-nonstoichiometric $La_{2-x}NiO_{4+\delta}$ (x = 0-0.1) oxides, *J. Mater. Chem. A*, 2015, **3**, 6501–6508.

28 X. Huang, T. H. Shin, J. Zhou and J. T. S. Irvine, Hierarchically nanoporous $La_{1.7}Ca_{0.3}CuO_{4-\delta}$ and $La_{1.7}Ca_{0.3}Ni_xCu_{1-x}O_{4-\delta}$ ($0.25 \leq x \leq 0.75$) as potential cathode materials for IT-SOFCs, *J. Mater. Chem. A*, 2015, **3**, 13468–13475.

29 J. Zhou, G. Chen, K. Wu and Y. Cheng, The performance of $La_{0.6}Sr_{1.4}MnO_4$ layered perovskite electrode material for intermediate temperature symmetrical solid oxide fuel cells, *J. Power Sources*, 2014, **270**, 418–425.

30 Y. Jiang, F. Chen and C. Xia, A review on cathode processes and materials for electro-reduction of carbon dioxide in solid oxide electrolysis cells, *J. Power Sources*, 2021, **493**, 229713.

31 D. Neagu, T. S. Oh, D. N. Miller, H. Ménard, S. M. Bukhari, S. R. Gamble, R. J. Gorte, J. M. Vohs and J. T. S. Irvine, Nano-socketed nickel particles with enhanced coking resistance grown in situ by redox exsolution, *Nat. Commun.*, 2015, **6**, 8120.

32 W. Wang, H. Li, C. Y. Regalado Vera, J. Lin, K. Y. Park, T. Lee, D. Ding and F. Chen, Improving the performance for direct electrolysis of CO_2 in solid oxide electrolysis cells with a $Sr_{1.9}Fe_{1.5}Mo_{0.5}O_{6-\delta}$ electrode via infiltration of Pr_6O_{11} nanoparticles, *J. Mater. Chem. A*, 2023, **11**, 9039–9048.

33 A. Orera, A. Betato, J. Silva-Treviño, Á. Larrea and M. Á. Laguna-Bercero, Advanced metal oxide infiltrated electrodes for boosting the performance of solid oxide cells, *J. Mater. Chem. A*, 2022, **10**, 2541–2549.

34 C. Zhu, S. Hou, L. Hou and K. Xie, Perovskite $SrFeO_{3-\delta}$ decorated with Ni nanoparticles for high temperature carbon

dioxide electrolysis, *Int. J. Hydrogen Energy*, 2018, **43**, 17040–17047.

35 R. Xing, Y. Wang, Y. Zhu, S. Liu and C. Jin, Co-electrolysis of steam and CO_2 in a solid oxide electrolysis cell with $La_{0.75}Sr_{0.25}Cr_{0.5}Mn_{0.5}O_{3-\delta}$–Cu ceramic composite electrode, *J. Power Sources*, 2015, **274**, 260–264.

36 S. Xu, S. Chen, M. Li, K. Xie, Y. Wang and Y. Wu, Composite cathode based on Fe-loaded LSCM for steam electrolysis in an oxide-ion-conducting solid oxide electrolyser, *J. Power Sources*, 2013, **239**, 332–340.

37 L. Ye, K. Zhu, Y. Jiang, S. Zhang, R. Peng and C. Xia, Carbon dioxide reduction processes on a samarium doped ceria electrocatalyst with exsolved Fe particles, *J. Mater. Chem. A*, 2023, 10646–10658.

38 Y. Jiang, L. Ye, S. Zhang and C. Xia, Doped ceria with exsolved Fe^0 nanoparticles as a Sr-free cathode for CO_2 electrolysis in SOECs at reduced temperatures, *J. Mater. Chem. A*, 2022, **10**, 9380–9383.

39 X. Sun, Y. Ye, M. Zhou, H. Chen, Y. Li, P. Chen, D. Dong, Y. Ling, M. Khan and Y. Chen, Layered-perovskite oxides with: In situ exsolved Co-Fe alloy nanoparticles as highly efficient electrodes for high-temperature carbon dioxide electrolysis, *J. Mater. Chem. A*, 2022, **10**, 2327–2335.

40 Y. S. Chung, T. Kim, T. H. Shin, H. Yoon, S. Park, N. M. Sammes, W. B. Kim and J. S. Chung, In situ preparation of a $La_{1.2}Sr_{0.8}Mn_{0.4}Fe_{0.6}O_4$ Ruddlesden-Popper phase with exsolved Fe nanoparticles as an anode for SOFCs, *J. Mater. Chem. A*, 2017, **5**, 6437–6446.

41 S. Park, Y. Kim, Y. Noh, T. Kim, H. Han, W. Yoon, J. Choi, S. H. Yi, W. J. Lee and W. B. Kim, A sulfur-tolerant cathode catalyst fabricated with in situ exsolved CoNi alloy nanoparticles anchored on a Ruddlesden-Popper support for CO_2 electrolysis, *J. Mater. Chem. A*, 2020, **8**, 138–148.

42 S. Park, Y. Kim, H. Han, Y. S. Chung, W. Yoon, J. Choi and W. B. Kim, In situ exsolved Co nanoparticles on Ruddlesden-Popper material as highly active catalyst for CO_2 electrolysis to CO, *Appl. Catal. B Environ.*, 2019, **248**, 147–156.

43 H. Lv, L. Lin, X. Zhang, D. Gao, Y. Song, Y. Zhou, Q. Liu, G. Wang and X. Bao, In situ exsolved $FeNi_3$ nanoparticles on nickel doped $Sr_2Fe_{1.5}Mo_{0.5}O_{6-\delta}$ perovskite for efficient electrochemical CO_2 reduction reaction, *J. Mater. Chem. A*, 2019, **7**, 11967–11975.

44 B. H. Toby and R. B. Von Dreele, GSAS-II: The genesis of a modern open-source all purpose crystallography software package, *J. Appl. Crystallogr.*, 2013, **46**, 544–549.

45 Y. Zhang, N. Xu, Q. Tang and K. Huang, Intermediate Temperature Solid Oxide Cell with a Barrier Layer Free Oxygen Electrode and Phase Inversion Derived Hydrogen Electrode, *J. Electrochem. Soc.*, 2022, **169**, 034516.

46 J. Zhang, M. R. Gao and J. L. Luo, In Situ Exsolved Metal Nanoparticles: A Smart Approach for Optimization of Catalysts, *Chem. Mater.*, 2020, **32**, 5424–5441.

47 X. Xiong, J. Yu, X. Huang, D. Zou, Y. Song, M. Xu, R. Ran, W. Wang, W. Zhou and Z. Shao, Slightly ruthenium doping enables better alloy nanoparticle exsolution of perovskite anode for high-performance direct-ammonia solid oxide fuel cells, *J. Mater. Sci. Technol.*, 2022, **125**, 51–58.

48 B. K. Park and S. A. Barnett, Boosting solid oxide fuel cell performance: Via electrolyte thickness reduction and cathode infiltration, *J. Mater. Chem. A*, 2020, **8**, 11626–11631.

49 M. Y. Lu, R. Scipioni, B. K. Park, T. Yang, Y. A. Chart and S. A. Barnett, Mechanisms of PrO_x performance enhancement of oxygen electrodes for low and intermediate temperature solid oxide fuel cells, *Mater. Today Energy*, 2019, **14**, 100362.

50 S. Liu, K. T. Chuang and J. L. Luo, Double-Layered Perovskite Anode with in Situ Exsolution of a Co-Fe Alloy to Cogenerate Ethylene and Electricity in a Proton-Conducting Ethane Fuel Cell, *ACS Catal.*, 2016, **6**, 760–768.

51 Y. Bu, Q. Zhong, D. Xu and W. Tan, Redox stability and sulfur resistance of $Sm_{0.9}Sr_{0.1}Cr_xFe_{1-x}O_{3-\delta}$ perovskite materials, *J. Alloys Compd.*, 2013, **578**, 60–66.

52 M. C. Biesinger, B. P. Payne, A. P. Grosvenor, L. W. M. Lau, A. R. Gerson and R. S. C. Smart, Resolving surface chemical states in XPS analysis of first row transition metals, oxides and hydroxides: Cr, Mn, Fe, Co and Ni, *Appl. Surf. Sci.*, 2011, **257**, 2717–2730.

53 D. H. Yoon, Y. J. Tak, S. P. Park, J. Jung, H. Lee and H. J. Kim, Simultaneous engineering of the interface and bulk layer of Al/sol-NiO_x/Si structured resistive random access memory devices, *J. Mater. Chem. C*, 2014, **2**, 6148–6154.

54 C. Su, W. Wang, R. Ran, Z. Shao, M. O. Tade and S. Liu, Renewable acetic acid in combination with solid oxide fuel cells for sustainable clean electric power generation, *J. Mater. Chem. A*, 2013, **1**, 5620–5627.

55 Y. Xie, J. Xiao, D. Liu, J. Liu and C. Yang, Electrolysis of Carbon Dioxide in a Solid Oxide Electrolyzer with Silver-Gadolinium-Doped Ceria Cathode, *J. Electrochem. Soc.*, 2015, **162**, F397–F402.

56 X. Xi, J. Liu, Y. Fan, L. Wang, J. Li, M. Li, J. L. Luo and X. Z. Fu, Reducing d-p band coupling to enhance CO_2 electrocatalytic activity by Mg-doping in $Sr_2FeMoO_{6-\delta}$ double perovskite for high performance solid oxide electrolysis cells, *Nano Energy*, 2021, **82**, 105707.

57 Y. Hou, L. Wang, L. Bian, Y. Wang, K. Chou and R. V. Kumar, High-performance $La_{0.3}Sr_{0.7}Fe_{0.9}Ti_{0.1}O_{3-\delta}$ as fuel electrode for directly electrolyzing CO_2 in solid oxide electrolysis cells, *Electrochim. Acta*, 2020, **342**, 1–9.

58 H. Lv, L. Lin, X. Zhang, R. Li, Y. Song, H. Matsumoto, N. Ta, C. Zeng, Q. Fu, G. Wang and X. Bao, Promoting exsolution of RuFe alloy nanoparticles on $Sr_2Fe_{1.4}Ru_{0.1}Mo_{0.5}O_{6-\delta}$ via repeated redox manipulations for CO_2 electrolysis, *Nat. Commun.*, 2021, **12**, 5665.

59 Y. Jiang, Y. Yang, C. Xia and H. J. M. Bouwmeester, $Sr_2Fe_{1.4}Mn_{0.1}Mo_{0.5}O_{6-\delta}$ perovskite cathode for highly efficient CO_2 electrolysis, *J. Mater. Chem. A*, 2019, **7**, 22939–22949.

60 Y. Tian, H. Zheng, L. Zhang, B. Chi, J. Pu and J. Li, Direct Electrolysis of CO_2 in Symmetrical Solid Oxide Electrolysis Cell Based on $La_{0.6}Sr_{0.4}Fe_{0.8}Ni_{0.2}O_{3-\delta}$ Electrode , *J. Electrochem. Soc.*, 2018, **165**, F17–F23.

61 Y. Li, B. Hu, C. Xia, W. Q. Xu, J. P. Lemmon and F. Chen, A novel fuel electrode enabling direct CO_2 electrolysis with excellent and stable cell performance, *J. Mater. Chem. A*, 2017, **5**, 20833–20842.

62 Y. Tian, L. Zhang, Y. Liu, L. Jia, J. Yang, B. Chi, J. Pu and J. Li, A self-recovering robust electrode for highly efficient CO_2 electrolysis in symmetrical solid oxide electrolysis cells, *J. Mater. Chem. A*, 2019, **7**, 6395–6400.

63 S. Liu, Q. Liu and J. L. Luo, Highly Stable and Efficient Catalyst with in Situ Exsolved Fe-Ni Alloy Nanospheres Socketed on an Oxygen Deficient Perovskite for Direct CO_2 Electrolysis, *ACS Catal.*, 2016, **6**, 6219–6228.

64 K. R. Cooper and M. Smith, Electrical test methods for on-line fuel cell ohmic resistance measurement, *J. Power Sources*, 2006, **160**, 1088–1095.

65 Y. Li, J. Zhou, D. Dong, Y. Wang, J. Z. Jiang, H. Xiang and K. Xie, Composite fuel electrode $La_{0.2}Sr_{0.8}TiO_{3-\delta}$-$Ce_{0.8}Sm_{0.2}O_{2-\delta}$ for electrolysis of CO_2 in an oxygen-ion conducting solid oxide electrolyser, *Phys. Chem. Chem. Phys.*, 2012, **14**, 15547–15553.

66 P. Caliandro, A. Nakajo, S. Diethelm and J. Van herle, Model-assisted identification of solid oxide cell elementary processes by electrochemical impedance spectroscopy measurements, *J. Power Sources*, 2019, **436**, 226838.